The Plant Journal (2008) **53**, 186–196 doi: 10.1111/j.1365-313X.2007.03306.x

TECHNICAL ADVANCE

Variable-angle epifluorescence microscopy: a new way to look at protein dynamics in the plant cell cortex

Catherine A. Konopka and Sebastian Y. Bednarek*

Program in Cell and Molecular Biology and Department of Biochemistry, University of Wisconsin – Madison, 433 Babcock Drive, Madison, WI 53706, USA

Received 4 June 2007; revised 17 August 2007; accepted 28 August 2007.
*For correspondence (fax +1 608 262 3453; e-mail bednarek@biochem.wisc.edu).

Summary

Live-cell microscopy imaging of fluorescent-tagged fusion proteins is an essential tool for cell biologists. Total internal reflection fluorescence microscopy (TIRFM) has joined confocal microscopy as a complementary system for the imaging of cell surface protein dynamics in mammalian and yeast systems because of its high temporal and spatial resolution. Here we present an alternative to TIRFM, termed variable-angle epifluorescence microscopy (VAEM), for the visualization of protein dynamics at or near the plasma membrane of plant epidermal cells and root hairs in whole, intact seedlings that provides high-signal, low-background and near real-time imaging. VAEM uses highly oblique subcritical incident angles to decrease background fluorophore excitation. We discuss the utilities and advantages of VAEM for imaging of fluorescent fusion-tagged marker proteins in studying cortical cytoskeletal and membrane proteins. We believe that the application of VAEM will be an invaluable imaging tool for plant cell biologists.

Keywords: live cell imaging, fluorescence microscopy, laser scanning confocal microscopy, TIRFM, cytoskeletal and membrane protein dynamics, VAEM.

Introduction

Fixed and live-cell fluorescence microscopy are invaluable for imaging protein localization and dynamics. With the development of new technologies for fluorescent labeling of proteins *in vivo* and the introduction of new imaging advancements comes a new or refined understanding of biological systems. The application of laser scanning confocal microscopy (LSCM) and spinning disk confocal microscopy technologies has provided enormous detail and insight into cellular dynamics; nevertheless confocal microscopy has some limitations, including a *z*-resolution limit, large areas of illumination which could damage live cells over long imaging intervals and, in the case of LSCM, relatively long capture times, which is problematic for capturing highly dynamic events such as vesicle trafficking and fusion.

Total internal reflection fluorescence microscopy (TIRFM), also called evanescent wave fluorescence (EF) microscopy, is complementary to confocal microscopy for imaging events with fast dynamics at or near the cell surface. Total internal reflection fluorescence microscopy has been utilized for over 20 years (Axelrod, 2001); however, it has only recently become more widely applied to studies of biological systems as commercially produced modular imaging systems have become available along with the development of fluorescent protein tags such as green fluorescent protein (GFP) and its spectral derivatives.

In contrast to standard epifluorescence microscopy, TIRFM relies on the total internal reflection of the illuminating laser light. During TIRFM the incident angle of the excitation laser is adjusted, such that a critical angle of illumination is achieved at the interface between two media in which the index of refraction of the second medium is lower than that of the first medium (most often glass to water or cytoplasm; Figure 1). This results in the production of an electromagnetic field (i.e. an evanescent wave of illumination) of the same frequency as the incident light within the sample (see,

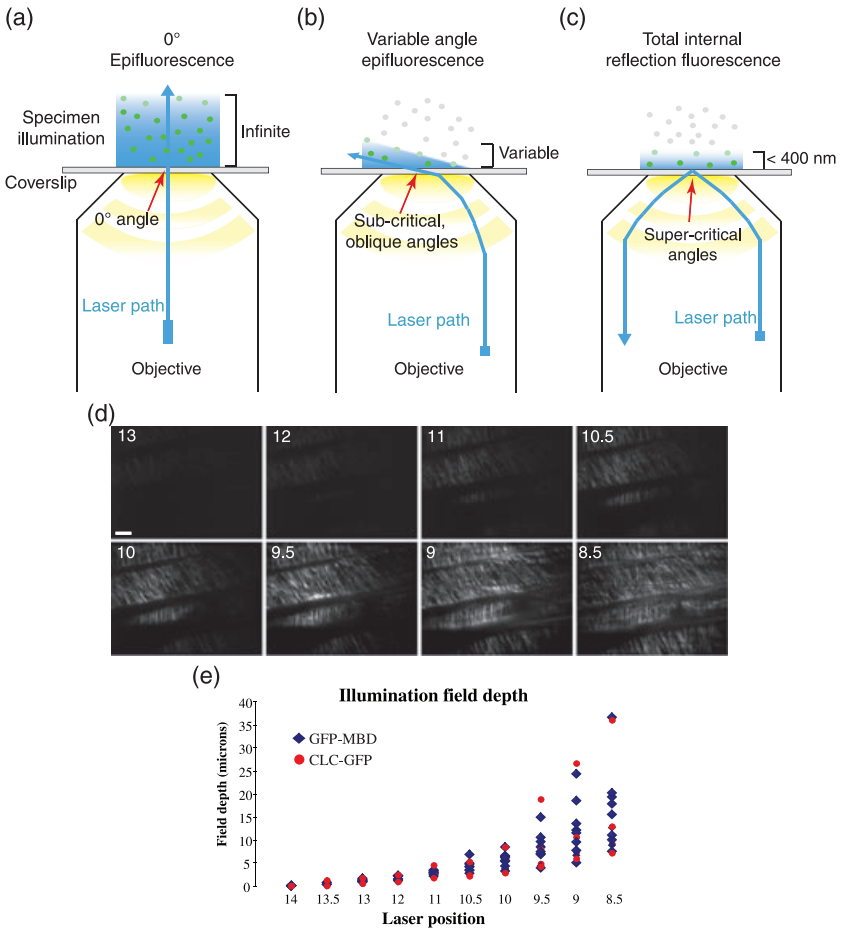

Figure 1. Variable-angle epifluorescence allows high signal to noise imaging close to the cell surface.
(a–c) Schematic of the laser path (blue line) in standard laser epifluorescence (a), variable-angle epifluorescence (VAEM; b), and total internal reflection fluorescence (TIRF; c). Variable-angle epifluorescence uses a range of subcritical angles of incidence resulting in slanted side band illumination and variable depth of illumination. Total internal reflection fluorescence uses a small range of critical and super-critical incident angles resulting in an illumination depth of 400 nm or less. Green dots represent excited fluorophores and grey dots represent un-excited fluorophores. The laser path through the objective was controlled by altering the position of reflective mirrors in the Nikon TIRF attachment.
(d) A representative microtubule-binding domain (MBD)-GFP-expressing root imaged at each laser position graphed in (e). The number position in each frame corresponds to the laser position in the graph.
(e) Fourteen roots expressing either GFP-MBD (blue diamonds) or clathrin light chain (CLC)-GFP (red circles) were imaged at 10 different laser positions producing 10 different decreasing angles of incidence. Position 14 corresponds to a refracted angle in which no MBD-GFP or CLC-GFP fluorescence could be visualized. Position numbers are in millimeters representing the mirror position in the Nikon T-FL-TIRF attachment. Changes in mirror position do not correspond linearly to the changes in either the angle of incidence or refraction. The depth of illumination was determined at each laser position relative to the fluorescent cortical microtubules. Notice that at the smaller angles of incidence (positions 10–8.5), cells farther away from the coverslip become illuminated, illustrating the increase in illumination field depth. Bars = 5 μm.

for review, Axelrod, 2001; Schneckenburger, 2005). The evanescent wave decays exponentially, exciting only fluorophores within approximately 400 nm of the glass coverslip. This creates a field of focus with a high signal-to-noise ratio (SNR) for imaging objects near the coverslip, thereby making TIRFM an ideal tool for visualizing cellular events near the cell surface. Photobleaching and cellular damage is less problematic in TIRFM than in LSCM and spinning disk confocal microscopy as only a subset of fluorophores are illuminated during imaging. Total internal reflection fluorescence microscopy has been used to visualize events such as clathrin-dependent endocytosis (Merrifield *et al.*, 2002), caveolae trafficking (Tagawa *et al.*, 2005), actin dynamics (Popp *et al.*, 2006), insulin granule release (Tsuboi *et al.*, 2005), calcium ion channel activity (Demuro and Parker, 2004) and substrate–receptor binding (Hellen and Axelrod, 1991). In addition, TIRFM has been combined with other microscopy techniques such as fluorescence recovery after photobleaching (FRAP; Sund and Axelrod, 2000), fluorescence resonance energy transfer (FRET; Riven *et al.*, 2003) and epifluorescence (Kaksonen *et al.*, 2005) to further study protein dynamics at the cell surface.

Due to the exponential decay of the evanescent wave produced during TIRFM, imaging of fluorescent molecules in

deeper areas of mammalian cells is limited. In addition, the application of TIRFM to the study of plant and fungal cells, which have cells walls and do not readily adhere well to glass surfaces, is not straightforward. Total internal reflection fluorescence microscopy has been applied to the study of endocytosis in *Saccharomyces cerevisae* in which the cells have been immobilized on the coverslip using concanavalin A (Kaksonen *et al.*, 2005) or lysine (Newpher *et al.*, 2005). However, it is not clear if the thickness or other properties of the yeast cell wall alter the quality of the TIRF imaging. The thickness of the *Saccharomyces* cell wall has been estimated to range from 0.11 μm (Holzel and Lamprecht, 1992) up to 0.26 μm (Gaskova *et al.*, 1998), approaching the limitation of TIRFM, if TIR is occurring at the coverslip interface. The thickness of plant cell walls varies even more widely and differs between plant species, cell types, plant age, growth status, and hydration level. Indeed, the width of the outer walls of plant epidermal cells is variable; they often measure over 0.5 μm thick (M. Otegui, University of Wisconsin-Madison, USA, personal communication), well beyond the theoretical penetration depth of an evanescent wave initiating from the glass coverslip. In addition, plant cell walls, depending upon their environment and developmental fate, are likely to have variable indices of refraction, making the path of incident light difficult to predict. It is not surprising, then, that the only reported studies utilizing TIRFM in plant research to date have been applied to investigate the *in vitro* dynamics of the plant actin cytoskeleton (Michelot *et al.*, 2005, 2006) and the *in vivo* analysis of pollen tube growth near the growing tip where the cell wall is still immature (Wang *et al.*, 2006). To our knowledge, TIRFM has not been used to study cortical protein dynamics in any intact multicellular organism. Here we describe an alternative use of TIRFM imaging systems to perform what we call variable-angle epifluorescence microscopy (VAEM). This application relies on the use of oblique (i.e. non-perpendicular), subcritical incident angles of the laser to image the dynamics of fluorescent-tagged cortical-associated proteins in plant cells (Figure 1). Variable-angle epifluorescence microscopy combines the high SNR and near real-time imaging of TIRFM with the illumination depth of epifluorescence to view protein and organelle dynamics at and near the plasma membrane in epidermal cells of intact plants.

Results and discussion

Utilization and analysis of VAEM for imaging of plant protein and organelle dynamics

In this paper, we have characterized the use of VAEM imaging of plant epidermal cells expressing various fluorescent-tagged fusion proteins using an inverted Nikon Eclipse TE2000-U microscope equipped with the Nikon T-FL-TIRF attachment (http://www.nikon.com/). The Nikon T-FL-TIRF attachment, which lies upstream of the objective, consists of a set of adjustable reflective mirrors controlling the path of the laser into the 100× TIRF objective and the distance of the laser from the optical axis (for details see Figure 1a and Experimental procedures). No adjustments were made to the microscope to switch between TIRFM and VAEM modes. Only the orientation of the reflective mirrors in the T-FL-TIRF attachment was varied to produce different angles of incidence of the laser. Importantly, we have confirmed that VAEM can be performed using other TIRFM imaging platforms that employ an adjustable laser path and a TIRF objective (data not shown).

Just as in TIRFM, the incident angle of the illuminating laser in VAEM was greater than zero degrees (perpendicular to the slide; Figure 1a), but unlike TIRFM (Figure 1c), subcritical angles were utilized (Figure 1b). At the highest oblique, yet subcritical, incident laser angle the light was refracted so that the field of illumination was narrow (Figure 1b), yielding a high SNR for visualizing events at or near the plasma membrane of intact cells. Figure 1(d) illustrates the changes in imaging of cortical microtubules (MTs) labeled with the GFP-tagged MT-binding domain (GFP-MBD) from MAP4 (Granger and Cyr, 2001) and the inclusion of out-of-focus fluorescence as the angle of incidence of the laser was decreased. The refracted light path created a slanted side band of illumination above the coverslip, resulting in a variable depth of the illumination field across the imaged area (Figure 1b). In principle the illumination penetration depth is infinite, but as only a limited area was imaged, the field depth is a function of the distance from the optical axis (Figure 1a). The difference in field depth across an image was only significant at very high refraction angles (Figure 1d, positions 10.5–13). The non-fluorescent areas of the images at high angles of refraction were a result of less penetration of incident light to those areas, which were farther away from the coverslip. The numbered positions refer to millimeters, representing the mirror alignment in the Nikon T-FL-TIRF attachment. Changes in mirror position do not correspond linearly to changes in either angle of incidence or refraction. To determine the illumination field depth, we imaged cortical MTs labeled with GFP-MBD (Figure 1d,e) and the plasma membrane-associated clathrin light chain (CLC)–GFP (Figure 1e) at various angles of incidence and determined the illumination field depth. Green fluorescent protein-tagged CLC has been used to follow clathrin-dependent endocytosis in yeast and animal systems (Kaksonen *et al.*, 2005; Merrifield *et al.*, 2002) and has a discrete organization within the plasma membrane of these organisms. At the highest angle of incidence in which cortical MTs and CLC could be imaged (Figure 1d, position 13.5) the illumination depth ranged from 0.3 to 0.7 μm. Figure 1(e) summarizes the illumination field depth of 14 individual roots expressing GFP-MBD or CLC-GFP at 10 decreasing angles of incidence of illumination. A representative root

expressing GFP-MBD that was imaged at 10 mirror positions (8.5–13) is shown (Figure 1d). As the angle of incidence was decreased, the illumination field depth increased as well as the average fluorescence intensity of the images. Conversely, a greater angle of incidence gave less illumination depth and a concomitant decrease in background fluorescence. It should be noted that scattered light may have also contributed to the depth of penetration of the incident light. Using the conditions reported here, the images obtained using VAEM of cortical cytoskeletal and membrane protein dynamics with the highest SNR and fewest irregularities in intensity were obtained from cells closest to the coverslip with few projecting objects nearby (i.e. shed root caps, trichomes, root hairs, etc.) to disturb the planarity of the cell or root. For the remainder of this study we will use the term 'oblique' to describe the subcritical incident angles that resulted in the highest SNR for each individual fluorescent-tagged protein.

Comparison of VAEM and standard epifluorescence for imaging of root epidermal cells

To compare VAEM with standard epifluorescence, cytoskeletal arrays (Figure 2a,b), plasma membrane-localized proteins (Figure 2c–f) and organelles (Figure 3a–e) were imaged in expanding root epidermal cells with the angle of incidence of the laser at zero degrees (i.e. standard epifluorescence) and at near critical, oblique angles, which are discussed below. For all plant lines examined, the average intensity over the full image was greater when taken with an angle of incidence of zero degrees than with oblique angles, due to increased noise of background fluorescence from the

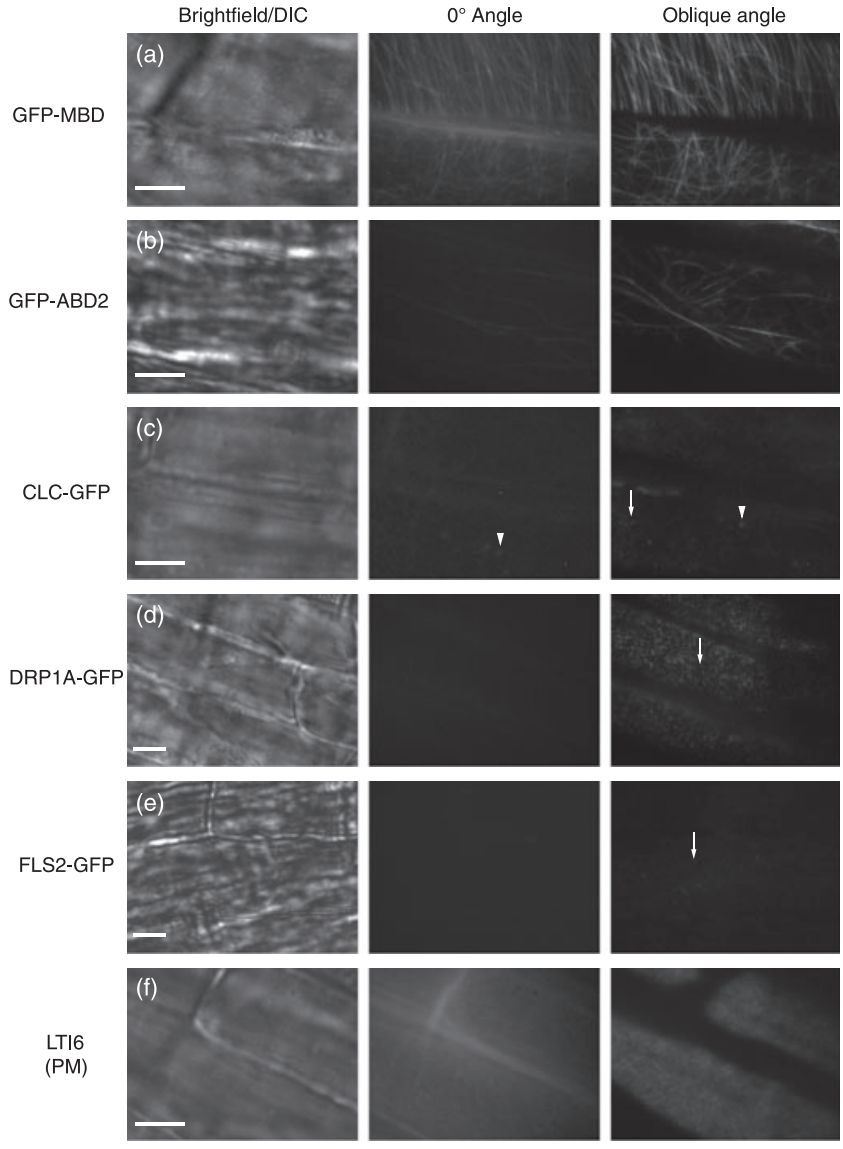

Figure 2. Cytoskeletal and plasma membrane proteins imaged with variable-angle epifluorescence microscopy (VAEM) at zero-angle and oblique angle illumination.
Root epidermal cells expressing GFP-microtubule-binding domain (MBD; a); GFP-ABD2 (b); clathrin light chain (CLC)-GFP (c); DRP1A-GFP (d); FLS2-GFP (e); LTI6b, a plasma membrane marker (f); imaged with brightfield, VAEM at zero-degree incident angle, and VAEM at oblique incident angles. Bars = 5 μm.

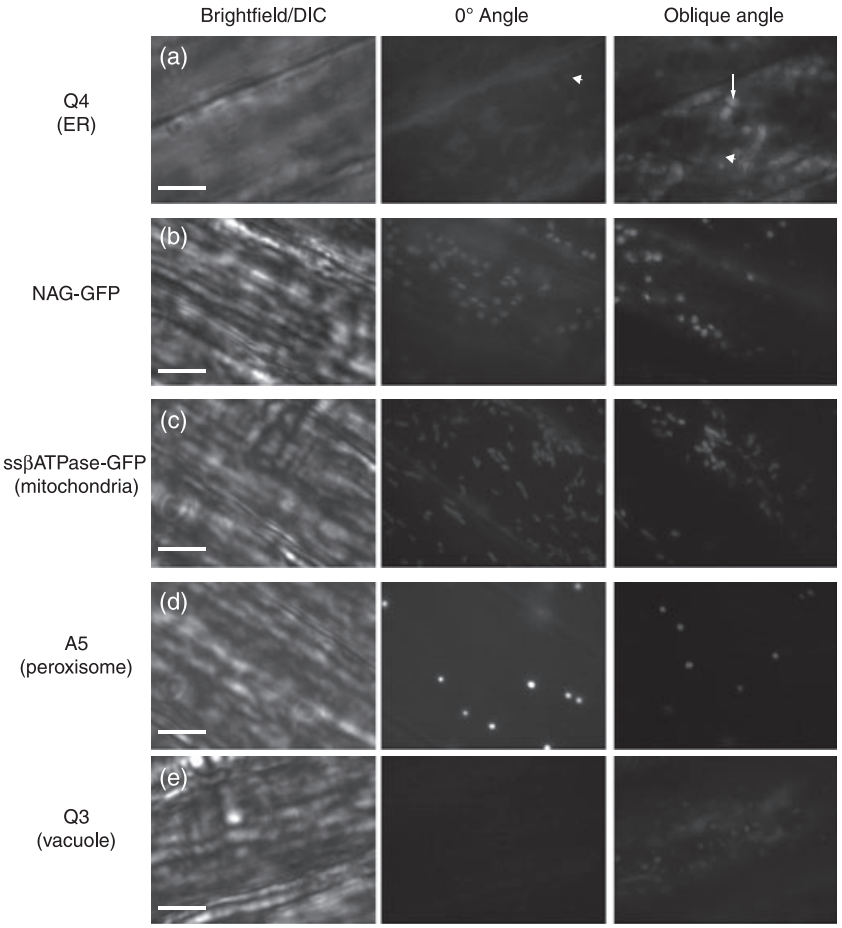

Figure 3. Organelle markers imaged with variable-angle epifluorescence microscopy (VAEM) at zero-degree and oblique angle illumination. Elongating root epidermal cells expressing Q4, an ER marker (a), NAG-GFP, a Golgi marker (b), ssβATPase-GFP (c), A5, a peroxisomal marker (d), or Q3, a tonoplast marker (e) imaged with brightfield VAEM at zero-degree incident angle, and VAEM at oblique incident angles. Bars = 5 μm.

transgenic and endogenous fluorophores in the plants and their environment.

Dynamic cytoskeletal arrays are apparent using VAEM

The greatest advantage of VAEM is the imaging of fluorescently labeled structures closest to the coverslip, as those will be the brightest and clearest. To follow the dynamics of MTs in root epidermal cells, plants expressing GFP-MBD were imaged. The GFP-MBD-labeled MTs were visible at oblique angles (Figure 2a). In time-lapse images of GFP-MBD-expressing cells (see Movie S1), microtubule growth and catastrophe events were apparent. The disordered organization of the MT array observed in the bottom cell (Figure 2a and Movie S1) was due to the formation of a root hair bulge in the trichoblast just outside the field of view, whereas the top cell was an atrichoblast and did not undergo reorganization of MTs as observed previously (Van Bruaene *et al.*, 2004). Similar cortical MT dynamics have been previously imaged in epidermal cells with high SNR using LSCM (Shaw *et al.*, 2003). The authors were able to visualize MT dynamics recording images every 3.85 sec. The time required for LSCM was sufficient to image MT growth and catastrophe; however, the increased time resolution afforded by VAEM may help to reveal more dynamic behaviors of cortical MTs or interactions with other proteins or organelles.

Imaging with an oblique angle also allowed the resolution of cortical actin cables decorated with the GFP-tagged Actin Binding Domain 2 (GFP-ABD2; Sheahan *et al.*, 2004), that were not detected with zero-degree illumination (Figure 2b, Movie S2). We were able to distinguish an average of 47.4 (±4.2) individual actin cables or filaments over 30 sec using oblique angle illumination. In contrast, we could only discern an average of 18.4 (±4.0) cables or filaments in the same epidermal root cell imaged using zero-degree illumination, despite a larger surface area of the cell illuminated. Sheahan *et al.* (2004) imaged GFP-ABD2-labeled actin dynamics in leaf pavement cells via LSCM every 1.6–6 sec. With this time resolution, the authors noted that the F-actin network dynamics consists of many filaments undergoing small movements. Actin filaments in root epidermal cells imaged with VAEM had similar contributions to network dynamics (Movie S2). The ability to resolve fine, dynamic actin structures is especially important for studying the

control mechanisms in tip growth in root hairs and pollen tubes. We have illustrated the power of VAEM for visualizing actin and MT dynamics in growing root hairs (see below).

Utilization of VAEM for visualization of plasma membrane protein dynamics and organization

In addition to the imaging of cortical cytoskeletal arrays, VAEM is also well suited for the visualization of plasma membrane protein dynamics. As shown in Figure 2(c) and Movie S3, this is illustrated by examining the localization and dynamics of CLC-GFP. The CLC has a punctate distribution within the plasma membrane of yeast and mammalian cells (Kaksonen *et al.*, 2005; Merrifield *et al.*, 2002). Likewise, CLC-GFP also formed discrete foci at the plasma membrane in root epidermal cells (Figure 2c, arrow; Movie S3). Clathrin light chain-GFP also labeled internal organelles (Figure 2c, arrowhead), which co-localized with a Golgi marker (data not shown). Despite these brighter, out of focus structures, the CLC-GFP foci at the plasma membrane could be distinguished. When the incident angle of the 488 nm laser was decreased from near subcritical angles toward zero degrees the foci were completely lost in the background signal arising from organelle-localized CLC-GFP, cytoplasmic CLC-GFP and populations from surrounding cells.

To establish further the ability of VAEM to display plasma membrane protein dynamics, we imaged a functional GFP-tagged Dynamin Related Protein 1A (DRP1A-GFP), which localizes to the plasma membrane in root epidermal cells (Kang *et al.*, 2003). As mammalian dynamin 1 forms foci at the plasma membrane during clathrin-dependent endocytosis in mammalian cultured cells (Merrifield *et al.*, 2002), we imaged root epidermal cells expressing DRP1A-GFP with VAEM to determine if it was organized in a similar manner. Indeed, DRP1A-GFP was present at the plasma membrane in discrete and dynamic foci (Figure 2d, arrow; Movie S4). The DRP1A-GFP foci were brighter than those formed by CLC-GFP, most likely because the GFP-tagged DRP1A was the only source of DRP1A in the cell, whereas endogenous, unlabeled CLC incorporated into the GFP-decorated clathrin lattice in the CLC-GFP plants. Despite this brighter fluorescence, the DRP1A-GFP foci were still almost completely lost at zero-degree illumination due to background fluorescence originating from the cytoplasm and neighboring cells. The plasma membrane-associated DRP1A-GFP foci were previously not detected using LSCM (Kang *et al.*, 2003), rather with LSCM DRP1A appeared to have a diffuse distribution. Likewise, we were not able to readily observe the dynamics of CLC-GFP foci with LSCM (data not shown).

Similar to CLC-GFP and DRP1A-GFP, the bona fide endocytic cargo transmembrane protein FLS2-GFP (Robatzek *et al.*, 2006) was also distributed in a punctate manner as observed by VAEM (Figure 2e, arrow, and Movie S5). This was interesting, as mammalian and fungal plasma membrane receptors cluster prior to endocytosis and the FLS2-GFP foci may represent sites of endocytosis. Unlike CLC-GFP and DRP1A-GFP, however, FLS2-GFP also exhibited a diffuse distribution, much like that of the LTI6b plasma membrane marker (Figure 2f and Movie S6).

Suborganelle dynamics as visualized by VAEM

In addition to imaging protein dynamics at the plasma membrane and cell cortex, VAEM was also used to image both organelle movements and suborganelle microdomain dynamics deeper within the cell with high SNR and near real-time imaging. Cortical endoplasmic reticulum (ER) was visualized by VAEM with the ER membrane marker Q4 (Cutler *et al.*, 2000). One of the more striking features was both the presence of GFP-positive structures (Figure 3a, arrow) and depleted areas of ER fluorescence (Figure 3a, arrowhead, and Movie S7). The ER-GFP label-depleted areas could also be seen in zero-degree illumination, but the brighter structures were lost. These 'holes' could be analogous to the 'bubbles' described by Cutler *et al.* (2000) that were observed by LSCM using an unidentified GFP-labeled protein that is thought to be associated with the ER.

Golgi movements were visualized with *N*-acetyl glucosaminyl (NAG) transferase–GFP (Grebe *et al.*, 2003; Figure 3b and Movie S8). As has been reported previously, some Golgi stacks remained relatively motionless while others were actively transported, most likely via an actin-dependent mechanism as previously shown (Boevink *et al.*, 1998; daSilva *et al.*, 2004). Imaging with oblique angles gave only a slightly higher SNR than imaging with a zero-degree angle most likely because the GFP-NAG label was concentrated in the Golgi, which gave the organelle a high fluorescence intensity. Background fluorescence emanating from the Golgi in the same and neighboring cells (out-of-focus Golgi) was lower with oblique angles, which will be beneficial if co-labeling studies are required as any increase in background could mask a potential co-localization making VAEM more discriminatory than standard epifluorescence.

Variable-angle epifluorescence microscopy was also applied to the imaging of other organelles with similar image quality and SNR as observed for the Golgi. The GFP-labeled organelles in both the mitochondrial marker line (ssβATPase-GFP; Logan and Leaver, 2000) and the peroxisomal marker line (A5; Cutler *et al.*, 2000) had high fluorescence intensity compared with the plasma membrane and tonoplast (see below) because the fluorescent protein was concentrated within the organelle and not distributed over a large surface (Figure 3c, d and Movies S9 and S10). Interestingly, when using an oblique angle the peroxisome label appeared to be on the periphery of the peroxisome (described as a torus in Cutler *et al.*, 2000), but this was masked when using standard epifluorescence (Figure 3d). Changes in mitochondrial morphology at the cell cortex

were also visible at both imaging angles (Figure 3c and Movie S9). Morphological changes were recorded at each frame (every 0.5 sec), which would not have been resolved using the slower frame rates of LSCM.

Although VAEM was most useful for imaging highly dynamic events near the cortex of the cell, it was also used to observe tonoplast dynamics using the Q3 (DIP aquaporin) marker (Cutler *et al.*, 2000). In contrast to LSCM medial sections and descriptions of the Q3-labeled membrane, the fluorescence was not evenly distributed throughout the vacuolar membrane when observed with VAEM. With VAEM the Q3 marker (Figure 3e) appeared to be organized into domains within in the tonoplast. These 'domains' may be regions of vacuole membrane invagination. Time series (Movie S11) were reminiscent of glancing LSCM sections (Cutler *et al.*, 2000). The domains were not readily detected by standard epifluorescence and instead the fluorescence appeared evenly distributed across the tonoplast (Figures 3e, zero-degree illumination). Variable-angle epifluorescence microscopy could prove useful for studying tonoplast dynamics and its interactions with other organelles such as the pre-vacuolar compartment.

Comparison of the time resolution between VAEM and confocal microscopy imaging

As noted above VAEM is especially useful for imaging highly dynamic structures near or at the plasma membrane, making VAEM complementary to LSCM and scanning disk microscopy, which allow imaging deeper within specimens. Laser scanning confocal microscopy is the most widely available confocal technique and gives excellent SNR due to its ability to discard out-of-focus fluorescence. However, scanning individual pixels requires relatively long frame rates. Variable-angle epifluorescence microscopy imaging produced similar SNR to LSCM, but enabled additional time resolution. In the images and time series described above, all acquisition rates were two frames per second (fps). This is comparable with the fastest rates of LSCM for a standard 512×512 pixel resolution (maximum scan rates vary for different systems, but are in the range of 2–5 fps). The capture rate of 2 fps was used as a standard in this study to image both intense and dimmer fluorophores; nevertheless, VAEM microscopy can employ much higher acquisition rates than LSCM and is theoretically limited by the readout of the camera (10.4 fps for this study) and practically limited by the brightness of the fluorophore. Some of the brightest organelle markers, such as GFP-NAG and ssβATPase-GFP, could be imaged with exposure times of <20 msec, corresponding to a theoretical acquisition rate of 50 fps (data not show). This is within the range of spinning-disk confocal frame rates. Even faster rates could be obtained with VAEM by using more sensitive cameras or by lowering the resolution (data not shown), which would not be a concern when imaging large structures such as Golgi stacks, peroxisomes and mitochondria, but which may not be practical for following the dynamics of individual actin filaments.

VAEM can be used to visualize protein, organelle and cytoskeletal dynamics in various epidermal cell types

In addition to the imaging of root epidermal cells VAEM can be used to visualize protein localization and dynamics in other epidermal tissue cell types. We used the GFP-MBD line to follow MT dynamics in hypocotyl epidermal cells, leaf pavement cells, stomata and leaf trichomes. Like root cells, hypocotyl epidermal cells were readily imaged because of their large size and planar morphology, and cortical MTs were apparent using VAEM as with traditional microscopy techniques (Figure 4a). The variable and non-planar shape of leaf pavement cells and guard cells made it unfeasible to image an entire MT array in these cells (Figure 4b, c), as part of the array was not in the imaging plane. However, the low background fluorescence allowed us to follow microtubule dynamics without difficulty (Movie S12). Variable-angle epifluorescence microscopy was also applied to the imaging of leaf trichomes, which is one of the more difficult cell types to image due its cylindrical, three-dimensional structure. As in the other epidermal cell types, cortical MT arrays were clearly visible using the oblique imaging angles in VAEM (Figure 4d).

Using VAEM to image cytoskeletal dynamics in growing root hairs

Because of their highly polar nature of growth, root hairs and pollen tubes have been popular models for studying the mechanisms of polar cell expansion. A focal point of that research has been the study of microtubule and actin dynamics during tip growth, to which VAEM can be applied to further enhance our understanding. Root hairs are extremely sensitive to environmental changes and thus we have imaged root hairs without disturbing them by growing and imaging them through semi-solid agar on coverslips (adapted from Ketelaar *et al.*, 2004), allowing the roots and root hairs to grow towards the coverslip by growing the seedlings at an angle of 30° from the horizontal. This technique was very useful, as expanding root hairs could be imaged by LSCM for at least 2 h (CAK and SYB, in preparation). Variable-angle epifluorescence microscopy had advantages over TIRFM as it permitted the imaging of root hairs that elongated toward, but were not in contact with, the coverslip. The index of refraction of the semi-solid agar (measured at 1.33) was near that of water, and as a result the evanescent wave was not able to penetrate to the growing root hair. In addition, this growth method was unsuitable for standard epifluorescence as the surrounding agar reflected and scattered light, resulting in a much lower SNR (see

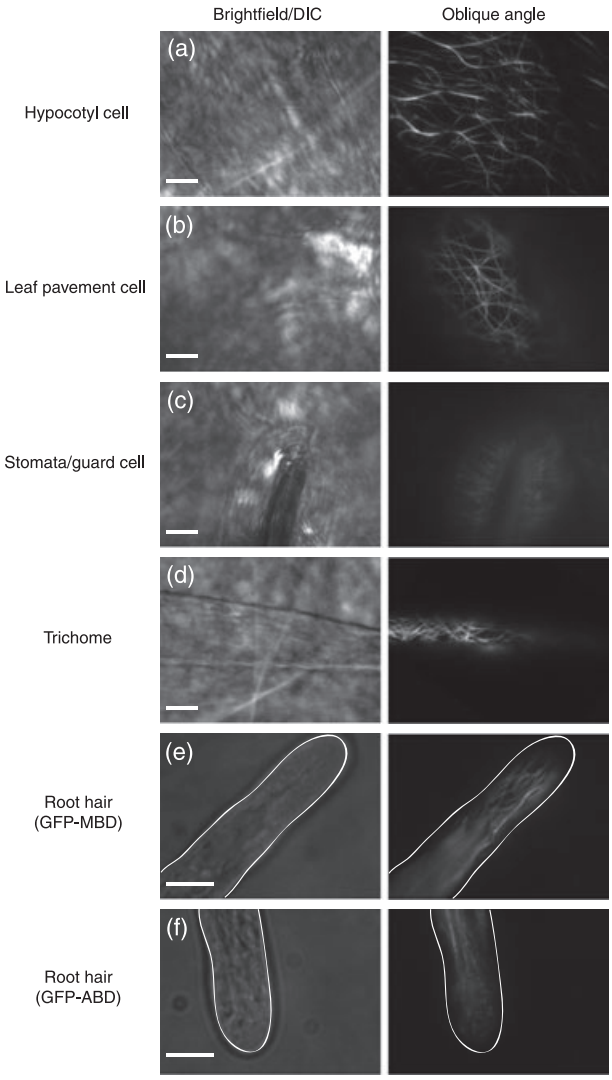

Figure 4. Variable-angle epifluorescence microscopy (VAEM) can be used to visualize fluorescent proteins in many epidermal cell types.
Epidermal cells expressing GFP-microtubule-binding domain (MBD; a–e) or GFP-ABD2 (f) were imaged with brightfield and VAEM at oblique incident angles: hypocotyls (a); cotyledon pavement cell (b); cotyledon guard cells forming an open stoma (c); trichome branch on first leaf (d); root hair growing in semi-solid medium (e, f). The white outline denotes the plasma membrane border of root hairs as determined by brightfield microscopy. Bars = 5 μm.

Movie S14b). Variable-angle epifluorescence microscopy, however, was quite valuable in visualizing cytoskeletal dynamics in the apical tip and flanks of growing root hairs (Figure 4e, f and Movies S13a, b and S14a).

To date it has not been clear whether MTs can penetrate into the vesicle-rich apical tip of root hairs. Microtubules were not detected in the tips of fixed cells by immunocytochemistry (Weerasinghe *et al.*, 2003) or live growing hairs using the GFP-MBD reporter in *Medicago truncatula* (Sieberer *et al.*, 2002) or Arabidopsis (Van Bruaene *et al.*, 2004). However, MTs were seen in the apical root hair tip in transmission electron micrographs in Arabidopsis (Galway *et al.*, 1997) and in live imaging of *M. truncatula* root hairs with EB1-GFP-labeled MTs (Timmers *et al.*, 2007). Microtubules in the root hair are highly dynamic, and it is possible that 4D LSCM did not have the time resolution to capture their presence (Van Bruaene *et al.*, 2004) or fully image their dynamics (Timmers *et al.*, 2007). Taking advantage of the faster imaging rates, and depth of view of VAEM we imaged MTs labeled with GFP-MBD in the apical tip of root hairs. Figure 4(e) and Movies 13(a, b) suggest that, although transient, MTs can extend into the apical tips of root hairs. The MTs present in the apical tip were more dynamic than the cortical MTs in the epidermal cells, some changing position every frame (0.5 sec). Both lateral displacement as well as MT growth contributed to the dynamic behavior. These subtle changes would be difficult to image using the slow frame rates of LSCM. Some MTs seemed to be stabilized at the plasma membrane of the apical tip and subsequently glided along the plasma membrane as previously described (Timmers *et al.*, 2007). The role of the apically localized MTs is still unknown; they may be required for targeting of polarity markers as suggested by Sieberer *et al.* (2002).

Actin dynamics are also critical during diffuse and tip growth, as the inhibition of actin dynamics by either depolymerization or stabilization can cause the cessation of tip growth altogether (Baluška *et al.*, 2000; Ketelaar *et al.*, 2003). High-resolution live-cell imaging of actin dynamics at the apical tip of root hairs is difficult to resolve using LSCM due to slower image capture times. Using VAEM we were able to visualize the actin dynamics at the tip in detail (Figure 4f and Movie 14a). The short actin filaments visualized with GFP-ABD2 had very limited lifetimes in the focal plane and were reminiscent of actin comets, dynamic actin structures that can propel objects (e.g. vesicles and endocytic pathogens) within the mammalian cytoplasm. As the root hairs had not been disturbed before or during imaging and the laser was illuminating the roots for <30 sec before capture, the short GFP-ABD2 labeled actin filaments probably represented actual filament dynamics during tip growth rather than imaging artifacts. The apical actin in tip-growing pollen tubes has often been described as a fine F-actin meshwork (Baluška *et al.*, 2000; Molendijk *et al.*, 2001; Šamaj *et al.*, 2002), and indeed the apical actin appeared as a hazy signal using zero-degree illumination (Movie S14b). It is possible that the F-actin mesh visualized with confocal microscopy (Baluška *et al.*, 2000) is actually composed of the highly dynamic actin filaments, and when captured at a slower rate, results in a visual meshwork of F-actin. Our studies suggest the presence of previously uncharacterized actin dynamics within the apical tip of a growing root hair and provide evidence of the usefulness of VAEM in imaging highly dynamic structures in tip-growing cells. Further use of VAEM with alternative actin probes may help to fully resolve this issue.

Concluding remarks

In this study, we have applied VAEM with a high SNR and frame rates to follow protein and organelle dynamics at and near the plasma membrane in whole, intact seedlings. Total internal reflection fluorescence imaging of protoplasts, which lack cell walls, is probably feasible; however, protoplasting may significantly alter the protein dynamics in the plasma membrane and the organization of the cell cortex. In addition, processes such as tip growth and polar growth in response to hormones and other stimuli cannot be studied using a non-polarized cultured cell. Total internal reflection fluorescence microscopy may also be applied to cultured plant cells that adhere to coverslips, but the properties of the plant cell wall may unpredictably affect the imaging. Thick epidermal outer cell walls have hindered the ability to visualize events at the plasma membrane via TIRFM, while in standard epifluorescence, fluorophore emissions from surrounding cells can mask details of protein and organelle dynamics. Using VAEM, an adaptation of TIRFM optics and instrumentation, with subcritical oblique angles, we have been able to observe phenomena both at the plasma membrane and in internal structures with a high SNR. We have combined the advantages of TIRFM (high SNR) and epifluorescence (imaging depth) with the frame rates of spinning disk confocal microscopy; and in doing so have illuminated new characteristics of commonly used fluorescent protein markers and cytoskeletal and plasma membrane protein dynamics.

Experimental procedures

Construction of fluorescent protein-tagged CLC binary expression vectors

The CLC-GFP was constructed as follows: A genomic fragment of At2g40060 was PCR amplified from BAC T28M21 (Arabidopsis Biological Resource Center, ABRC) with primers 5′-CTGCAGGAGTCGGAGATGATGATTATGATG-3′ (CLC for) and 5′-GAGCTCTTAGCAGCAGTAACTGCCTCAGTGGGC-3′, subcloned into pGEM T-easy (Promega, http://www.promega.com/), digested with *Pst*I and *Sac*I and subcloned into pPZP211 containing mGFP5 and nopaline synthase (NOS) terminator (Kang *et al.*, 2003).

Arabidopsis thaliana ecotype Wassilewskija wild-type plants were transformed with the fluorescent-tagged CLC constructs using the *Agrobacterium tumefaciens*-mediated floral dip method (Clough and Bent, 1998). Kanamycin-resistant transgenic plants were grown on solid medium (0.6% phytagar), ½ MS (Murishige and Skoog, 1962) medium (Caisson Labs, http://www.caissonlabs.com/) containing 40 μg ml^{-1} kanamycin (CLC-GFP) or on soil, sprayed once with 20 μg ml^{-1} ammonium glufosinate (CLC-mOrange; Liberty; http://www.bayercropscienceus.com).

Organelle, cytoskeletal and protein markers

Green fluorescent protein-ABD2 (Sheahan *et al.*, 2004) and the MBD-GFP (Granger and Cyr, 2001) lines were used to visualize cytoskeleton dynamics. The DRP1A-GFP was generated as previously described (Kang *et al.*, 2003). The A5, Q3, Q4 and LTI6b lines (Cutler *et al.*, 2000) were obtained from ABRC. The NAG-GFP (Grebe *et al.*, 2003) was kindly made available by B. Scheres (Universiteit Utrecht, Utrecht, The Netherlands), ssβATPase-GFP (Logan and Leaver, 2000) was a gift from D. Logan (University of St Andrews, St Andrews, UK) and FLS2-GFP (Robatzek *et al.*, 2006) was kindly given by S. Robatzek (Max-Planck-Institute for Plant Breeding Research, Cologne, Germany).

Actin filament quantification

An actin filament or cable was defined as a continuous line of fluorescence (GFP-ABD2) that could intersect other filaments or contact the membrane. Filaments were visually counted in five different frames of a 60-frame (30 sec) image series taken of an expanding root epidermal atrichoblast expressing GFP-ABD2. The number of filaments in the five frames was averaged and standard deviation taken.

Plant growth conditions

For visualization of epidermal cells, seeds were sterilized with 70% ethanol (EtOH), 0.1% TritonX-100/95% EtOH and plated on ½ MS + 1% phytoagar, stratified for 2–5 days and grown vertically under continuous light. For visualization of root hairs, seeds were sterilized as above and plated on coverslips coated with ½ MS + 0.5% agar (adapted from Ketelaar *et al.*, 2004). Three coverslips were placed into a 15 mm × 100 mm Petri dish, which was then sealed with two layers of parafilm (to prevent dehydration). The seedlings were allowed to germinate horizontally and then grown at 30° to the horizontal under continuous light.

Variable-angle epifluorescence imaging

Seedlings were transferred from vertically growing plates to a well containing ½ MS for ~10 sec and subsequently transferred to a glass slide with 150 μl ½ MS. A coverslip was placed over the root or entire seedling to ensure the fewest trapped air bubbles and excess liquid was drained from slide. The slide was placed on an inverted Nikon Eclipse TE2000-U microscope (with epifluorescence attachment) fitted with a Nikon 100× objective (numerical aperture 1.45 CFI Plan Apo TIRF) imaged with or without 1.5× intermediate magnification. Green fluorescent protein excited with a 488-nm argon laser (Melles Griot, http://www.mellesgriot.com/), with a maximum power output 30 mW and a beam width of 690 μm. Laser intensity was modulated using 2× or 8× neutral density filters when needed. The incident angle used was either zero degrees (perpendicular to the slide) or varied to give the highest SNR for each individual fluorescent line using a mirror-based Nikon T-FL-TIRF illuminator (Nikon), which allows the user to alter the path of the laser beam through the TIRF objective. Fluorescent emission was filtered through a 535/30 nm filter and captured using a CoolSnapES cooled CCD camera (Roper Scientific, http://www.roperscientific.com/) using Metamorph Imaging System Ver 6.2r6 (Molecular Devices, http://www.moleculardevices.com/). Exposure times were 500 msec unless otherwise noted and images were captured continuously for 30 sec or 60 sec. The image size was 696 × 520 pixels corresponding to 23.5 × 17.5 μm or 35.2 × 26.3 μm actual dimensions with or without the 1.5× intermediate magnification, respectively. Gray scale was set on a scale from 90 to 350 and average intensities ranged from 101 to 184.

For imaging root hairs the coverslips with seedlings grown in agar, as described above, were transferred directly to the inverted

microscope. One hundred and fifty microliters of ½ MS + 1% sucrose was added on top of the agar and the coverslip was covered with parafilm to prevent dehydration.

Illumination field depth analysis

Ten GFP-MBD-expressing and four CLC-GFP-expressing seedlings were grown and imaged as above with 1.5× intermediate magnification and image size 1392 × 1040 pixels corresponding to 46.9 × 35.0 μm actual dimensions. The incident angle at which no fluorescence was visible was noted and then subsequently decreased with regular changes in mirror position in the T-FL-TIRF attachment. At various laser positions, the maximal *Z*-position in which fluorescence emission could be detected was recorded as the illumination field depth. Field depth was measured at nine of the ten incident angles in five GFP-MBD seedlings and all ten incident angles in five GFP-MBD and the four CLC-GFP seedlings.

Acknowledgements

We thank T. Martin and members of his lab for help and extensive use of their epifluorescence-TIRF microscope. In addition, we thank T. Liu and F. M. Dunning in the labs of J. Weishaar and E. Chapman, respectively, for aid in the assessment of VAEM on their TIRF microscopes. We thank members of our lab, especially S. Backues, for critical reading of the manuscript and helpful discussions. This research was supported by funding to SYB from the USDA National Research Initiative Competitive Grants Program (project no. 2004-03411). CAK was supported by a Howard Hughes Medical Institute Predoctoral Fellowship and a National Institutes of Health, National Research Service Award T32 GM07215 from the National Institute of General Medical Sciences.

Supplementary Material

The following supplementary material is available for this article online:

Movie S1. Root epidermal cell expressing microtubule-binding domain (MBD)-GFP imaged with variable-angle epifluorescence microscopy at oblique angles.

Movie S2. Elongating root epidermal cell expressing the actin marker GFP-actin-binding domain (ABD), imaged with variable-angle epifluorescence microscopy at oblique angles.

Movie S3. Elongating root epidermal cell expressing clathrin light chain (CLC)-GFP imaged with variable-angle epifluorescence microscopy at oblique angles.

Movie S4. Elongating root epidermal cell expressing Dynamin Related Protein 1A (DRP1A)-GFP, imaged with variable-angle epifluorescence microscopy at oblique angles.

Movie S5. Elongating root epidermal cell expressing transmembrane protein FLS2-GFP imaged with variable-angle epifluorescence microscopy at oblique angles.

Movie S6. Elongating root epidermal cell expressing the general plasma membrane maker, LTI6b, imaged with variable-angle epifluorescence microscopy at oblique angles.

Movie S7. Elongating root epidermal cell expressing the endoplasmic reticulum marker, Q4, imaged with variable-angle epifluorescence microscopy at oblique angles.

Movie S8. Elongating root epidermal cell expressing the Golgi marker, GFP-NAG, imaged with variable-angle epifluorescence microscopy at oblique angles.

Movie S9. Elongating root epidermal cell expressing the mitochondrial marker, ssβATPase-GFP, imaged with variable-angle epifluorescence microscopy at oblique angles.

Movie S10. Elongating root epidermal cell expressing the peroxisome marker, A5, imaged with variable-angle epifluorescence microscopy at oblique angles.

Movie S11. Elongating root epidermal cell expressing the tonoplast marker, Q3, imaged with variable-angle epifluorescence microscopy at oblique angles.

Movie S12. Pavement cell on a cotyledon expressing microtubule-binding domain (MBD)-GFP imaged with variable-angle epifluorescence microscopy at oblique angles.

Movie S13. (a) Tip of root hair growing in semi-solid medium expressing microtubule-binding domain (MBD)-GFP imaged with variable-angle epifluorescence microscopy at oblique angles. (b) Tip of root hair growing in semi-solid medium expressing MBD-GFP imaged with variable-angle epifluorescence microscopy at oblique angles.

Movie S14. Tip of root hair growing in semi-solid medium expressing GFP-ABD2 imaged with variable-angle epifluorescence microscopy at oblique angles. (b) The same root hair as in (a) imaged with variable-angle epifluorescence microscopy at a zero-degree incident angle.

This material is available as part of the online article from http://www.blackwell-synergy.com.

References

Axelrod, D. (2001) Total internal reflection fluorescence microscopy in cell biology. *Traffic*, **2**, 764–774.

Baluška, F., Salaj, J., Mathur, J., Braun, M., Jasper, F., Šamaj, J., Chua, N.H., Barlow, P.W. and Volkmann, D. (2000) Root hair formation: F-actin-dependent tip growth is initiated by local assembly of profilin-supported F-actin meshworks accumulated within expansin-enriched bulges. *Dev. Biol.* **227**, 618–632.

Boevink, P., Oparka, K., Santa Cruz, S., Martin, B., Betteridge, A. and Hawes, C. (1998) Stacks on tracks: the plant Golgi apparatus traffics on an actin/ER network. *Plant J.* **15**, 441–447.

Clough, S.J. and Bent, A.F. (1998) Floral dip: a simplified method for Agrobacterium-mediated transformation of *Arabidopsis thaliana*. *Plant J.* **16**, 735–743.

Cutler, S.R., Ehrhardt, D.W., Griffitts, J.S. and Somerville, C.R. (2000) Random GFP::cDNA fusions enable visualization of subcellular structures in cells of Arabidopsis at a high frequency. *Proc. Natl Acad. Sci. USA*, **97**, 3718–3723.

Demuro, A. and Parker, I. (2004) Imaging the activity and localization of single voltage-gated Ca(2+) channels by total internal reflection fluorescence microscopy. *Biophys. J.* **86**, 3250–3259.

Galway, M.E., Heckman, J.W., Jr and Schiefelbein, J.W. (1997) Growth and ultrastructure of Arabidopsis root hairs: the rhd3 mutation alters vacuole enlargement and tip growth. *Planta*, **201**, 209–218.

Gaskova, D., Brodska, B., Herman, P., Vecer, J., Malinsky, J., Sigler, K., Benada, O. and Plasek, J. (1998) Fluorescent probing of membrane potential in walled cells: diS-C3(3) assay in *Saccharomyces cerevisiae*. *Yeast*, **14**, 1189–1197.

Granger, C.L. and Cyr, R.J. (2001) Spatiotemporal relationships between growth and microtubule orientation as revealed in living root cells of *Arabidopsis thaliana* transformed with green-fluorescent-protein gene construct GFP-MBD. *Protoplasma*, **216**, 201–214.

Grebe, M., Xu, J., Mobius, W., Ueda, T., Nakano, A., Geuze, H.J., Rook, M.B. and Scheres, B. (2003) Arabidopsis sterol endocytosis

involves actin-mediated trafficking via ARA6-positive early endosomes. *Curr. Biol.* **13**, 1378–1387.

Hellen, E. and Axelrod, D. (1991) Kinetics of epidermal growth factor/receptor binding on cells measured by total internal reflection/fluorescence recovery after photobleaching. *J. Fluoresc.* **1**, 113–128.

Holzel, R. and Lamprecht, I. (1992) Dielectric properties of yeast cells as determined by electrorotation. *Biochim. Biophys. Acta*, **1104**, 195–200.

Kaksonen, M., Toret, C.P. and Drubin, D.G. (2005) A modular design for the clathrin- and actin-mediated endocytosis machinery. *Cell*, **123**, 305–320.

Kang, B.H., Busse, J.S. and Bednarek, S.Y. (2003) Members of the Arabidopsis dynamin-like gene family, ADL1, are essential for plant cytokinesis and polarized cell growth. *Plant Cell*, **15**, 899–913.

Ketelaar, T., de Ruijter, N.C. and Emons, A.M. (2003) Unstable F-actin specifies the area and microtubule direction of cell expansion in Arabidopsis root hairs. *Plant Cell*, **15**, 285–292.

Ketelaar, T., Anthony, R.G. and Hussey, P.J. (2004) Green fluorescent protein-mTalin causes defects in actin organization and cell expansion in Arabidopsis and inhibits actin depolymerizing factor's actin depolymerizing activity in vitro. *Plant Physiol.* **136**, 3990–3998.

Logan, D.C. and Leaver, C.J. (2000) Mitochondria-targeted GFP highlights the heterogeneity of mitochondrial shape, size and movement within living plant cells. *J. Exp. Bot.* **51**, 865–871.

Merrifield, C.J., Feldman, M.E., Wan, L. and Almers, W. (2002) Imaging actin and dynamin recruitment during invagination of single clathrin-coated pits. *Nat. Cell. Biol.* **4**, 691–698.

Michelot, A., Guerin, C., Huang, S., Ingouff, M., Richard, S., Rodiuc, N., Staiger, C.J. and Blanchoin, L. (2005) The formin homology 1 domain modulates the actin nucleation and bundling activity of Arabidopsis FORMIN1. *Plant Cell*, **17**, 2296–2313.

Michelot, A., Derivery, E., Paterski-Boujemaa, R., Guerin, C., Huang, S., Parcy, F., Staiger, C.J. and Blanchoin, L. (2006) A novel mechanism for the formation of actin-filament bundles by a nonprocessive formin. *Curr. Biol.* **16**, 1924–1930.

Molendijk, A.J., Bischoff, F., Rajendrakumar, C.S., Friml, J., Braun, M., Gilroy, S. and Palme, K. (2001) Arabidopsis thaliana Rop GTPases are localized to tips of root hairs and control polar growth. *EMBO J.* **20**, 2779–2788.

Murishige, T. and Skoog, F. (1962) A revised medium for rapid growth and bioassays with tobacco tissue cultures. *Physiol. Plant.* **15**, 473–497.

Newpher, T.M., Smith, R.P., Lemmon, V. and Lemmon, S.K. (2005) In vivo dynamics of clathrin and its adaptor-dependent recruitment to the actin-based endocytic machinery in yeast. *Dev. Cell*, **9**, 87–98.

Popp, D., Yamamoto, A., Iwasa, M. and Maeda, Y. (2006) Direct visualization of actin nematic network formation and dynamics. *Biochem. Biophys. Res. Commun.* **351**, 348–353.

Riven, I., Kalmanzon, E., Segev, L. and Reuveny, E. (2003) Conformational rearrangements associated with the gating of the G protein-coupled potassium channel revealed by FRET microscopy. *Neuron*, **38**, 225–235.

Robatzek, S., Chinchilla, D. and Boller, T. (2006) Ligand-induced endocytosis of the pattern recognition receptor FLS2 in Arabidopsis. *Genes Dev.* **20**, 537–542.

Šamaj, J., Ovecka, M., Hlavacka, A. *et al.* (2002) Involvement of the mitogen-activated protein kinase SIMK in regulation of root hair tip growth. *EMBO J.* **21**, 3296–3306.

Schneckenburger, H. (2005) Total internal reflection fluorescence microscopy: technical innovations and novel applications. *Curr. Opin. Biotechnol.* **16**, 13–18.

Shaw, S.L., Kamyar, R. and Ehrhardt, D.W. (2003) Sustained microtubule treadmilling in Arabidopsis cortical arrays. *Science*, **300**, 1715–1718.

Sheahan, M.B., Staiger, C.J., Rose, R.J. and McCurdy, D.W. (2004) A green fluorescent protein fusion to actin-binding domain 2 of Arabidopsis fimbrin highlights new features of a dynamic actin cytoskeleton in live plant cells. *Plant Physiol.* **136**, 3968–3978.

Sieberer, B.J., Timmers, A.C., Lhuissier, F.G. and Emons, A.M. (2002) Endoplasmic microtubules configure the subapical cytoplasm and are required for fast growth of Medicago truncatula root hairs. *Plant Physiol.* **130**, 977–988.

daSilva, L.L., Snapp, E.L., Denecke, J., Lippincott-Schwartz, J., Hawes, C. and Brandizzi, F. (2004) Endoplasmic reticulum export sites and Golgi bodies behave as single mobile secretory units in plant cells. *Plant Cell*, **16**, 1753–1771.

Sund, S.E. and Axelrod, D. (2000) Actin dynamics at the living cell submembrane imaged by total internal reflection fluorescence photobleaching. *Biophys. J.* **79**, 1655–1669.

Tagawa, A., Mezzacasa, A., Hayer, A., Longatti, A., Pelkmans, L. and Helenius, A. (2005) Assembly and trafficking of caveolar domains in the cell: caveolae as stable, cargo-triggered, vesicular transporters. *J. Cell Biol.* **170**, 769–779.

Timmers, A.C., Vallotton, P., Heym, C. and Menzel, D. (2007) Microtubule dynamics in root hairs of *Medicago truncatula*. *Eur. J. Cell Biol.* **86**, 69–83.

Tsuboi, T., Ravier, M.A., Xie, H., Ewart, M.A., Gould, G.W., Baldwin, S.A. and Rutter, G.A. (2005) Mammalian exocyst complex is required for the docking step of insulin vesicle exocytosis. *J. Biol. Chem.* **280**, 25565–25570.

Van Bruaene, N., Joss, G. and Van Oostveldt, P. (2004) Reorganization and in vivo dynamics of microtubules during Arabidopsis root hair development. *Plant Physiol.* **136**, 3905–3919.

Wang, X., Teng, Y., Wang, Q., Li, X., Sheng, X., Zheng, M., Samaj, J., Baluska, F. and Lin, J. (2006) Imaging of dynamic secretory vesicles in living pollen tubes of Picea meyeri using evanescent wave microscopy. *Plant Physiol.* **141**, 1591–1603.

Weerasinghe, R.R., Collings, D.A., Johannes, E. and Allen, N.S. (2003) The distributional changes and role of microtubules in Nod factor-challenged Medicago sativa root hairs. *Planta*, **218**, 276–287.

